catalysts

MDPI

Article

Pre-Synthesized WO_3 Nanosheets via New Modified Thermal Exfoliation as a Route to Decouple Crystallinity from Loading in $Pt/WO_3/Al_2O_3$ Glycerol Hydrogenolysis Catalysts

Martino Fontana [1,*], Giuseppe Pipitone [2,*], Nadi Braidy [1], Mariangela Longhi [3], Carlo Pirola [3], Filippo Bossola [4], Ilaria Tornelli [3] and Federico Galli [1,*]

[1] Département de Génie Chimique et de Génie Biotechnologique, Université de Sherbrooke, 2500, Boul. de l'Université, Sherbrooke, QC J1K 2R1, Canada
[2] Dipartimento di Scienza Applicata e Tecnologia (DISAT), Politecnico di Torino, Corso Duca degli Abruzzi 24, 10129 Turin, Italy
[3] Dipartimento di Chimica, Universitá degli Studi di Milano, Via Golgi 19, 20133 Milan, Italy
[4] Consiglio Nazionale delle Ricerche—Istituto di Scienze e Tecnologie Chimiche "Giulio Natta", Via C. Golgi 19, 20133 Milan, Italy
* Correspondence: martino.fontana.1997@gmail.com (M.F.); giuseppe.pipitone@polito.it (G.P.); federico.galli@usherbrooke.ca (F.G.)

Abstract

The development of highly crystalline tungsten oxide nanomaterials remains challenging for catalytic applications due to the difficulty in achieving high phase purity without sacrificing metal oxide loading. This work addresses this limitation through an innovative fast hydrothermal synthesis at 100 °C for 4 h without autoclaves or surfactants, using citric acid as a critical structural directing agent. Such methodology reduces the synthesis time by 50–80% compared to existing hydrothermal routes. Citric acid was identified as the critical parameter controlling the nanosheet thickness (20 nm to 35 nm) and diameter (109 nm to 173 nm), acting as a coordinating ligand. The resulting nanosheets were used to prepare $Pt/WO_3/Al_2O_3$ catalysts with well-defined crystalline monoclinic WO_3 structures at 9.5% wt. loading. Normally, this phase is inaccessible by standard impregnation at equivalent loading. NH_3-TPD characterization confirmed that crystalline WO_3 generates strong acid sites absent in the reference wet impregnation catalyst. Glycerol hydrogenolysis tests revealed that the presence of monoclinic WO_3 reduces the average glycerol conversion rate by a factor of 3.8 and systematically shifts selectivity toward over-hydrogenolysis products (1-propanol and 2-propanol), despite identical WO_3 loading and surface densities below the literature optimum of 2.2 W atoms nm^{-2}. These results demonstrate that the WO_3 crystalline phase is a primary determinant of catalytic performance, without taking into account increased loading. Such demonstration will be useful for the rational design of selective glycerol hydrogenolysis catalysts.

Keywords: tungsten oxide; WO_3; nanosheets; hydrothermal synthesis; citric acid; exfoliation; EELS; XRD; $Pt/WO_3/Al_2O_3$; glycerol hydrogenolysis

Check for updates

Academic Editor: Benoît Louis

Received: 21 April 2026
Revised: 25 May 2026
Accepted: 26 June 2026
Published: 30 June 2026

Copyright: © 2026 by the authors. Licensee MDPI, Basel, Switzerland. This article is an open access article distributed under the terms and conditions of the Creative Commons Attribution (CC BY) license.

1. Introduction

Biodiesel production has been a rising industry in recent years. The IEA has estimated a worldwide biodiesel and hydrotreated vegetable oil (HVO) demand in 2030 of 215×10^9 L [1]. However, biodiesel production yields 10% wt. of glycerol as a by-product [2]. Glycerol is a chemical already produced by several other industrial processes,

such as propylene chlorination, oil hydrolysis in the soap industry, fermentation processes and so on [3]. Researchers have explored its valorization to other chemicals, particularly 1,2-propanediol (1,2-PD) and 1,3-propanediol (1,3-PD) transformation via the glycerol hydrogenolysis reaction [2,3]. Such large production of glycerol has motivated decades of work on catalyst design and optimization.

1,3-PD is a high-value industrial chemical (0.36 USD kg^{-1}) that is mainly used for polytrimethylene terephthalate (PTT) production. At present, 1,3-PD is produced through the Shell process, starting from ethylene oxide (produced from fossil oil), or from the innovative DuPont process, which derives it through the fermentation of corn oil but in much smaller volumes (10,000 t yr^{-1} against the 83,000 t yr^{-1} produced by Shell) [2].

Recent literature studies focus on the catalytic conversion of polyols such as glycerol or glyceraldehyde over supported metal catalysts, with particular attention to platinum-group metals, known for their hydrogenation activity and thermal stability [4]. However, achieving selective C–O bond cleavage at specific positions requires careful manipulation of the surface chemistry and acidity. Tungsten oxide, particularly in crystalline form, has emerged as a powerful promoter of platinum-catalyzed reactions, enhancing selectivity toward target products through oxygen vacancy formation and metal–support interactions that facilitate hydrogen spillover [5,6]. The strong metal–oxygen bond in tungsten oxide creates oxygen-deficient sites that stabilize reactive intermediates while simultaneously providing Brønsted acid functionality, creating a bifunctional surface architecture that is well suited to cascade reactions involving both dehydration and hydrogenation steps [6–8]. This catalyst can activate the H_2 and transfer it through hydrogen spillover on the WO_3 surface [9]. Meanwhile, the glycerol is coordinated with WO_3 and its C–O bond is cleaved; then, the activated H_2 migrates on glycerol to stabilize the intermediate, producing 1,2-PD or 1,3-PD.

Several authors have studied the structural properties of WO_3 to better understand its role in the selective production of 1,3-PD. N. Lei et al. demonstrated that a mixture of monoclinic WO_3 and polytungstate species at 12% wt. loading maximizes the 1,3-PD yield (up to 29%), suggesting that the crystallographic nature of WO_3, coupled with different loadings, critically determines catalytic performance [10]. These studies demonstrate that, at high WO_3 loadings (>12% wt.), the reaction shifts toward over-hydrogenolysis products due to excessive surface acidity generated by WO_3's increased surface density, as confirmed by other groups [5,10,11]. In fact, S. García-Fernández et al. found that the ideal surface density to produce 1,3-PD for WO_3 was at 2.2 W atoms nm^{-2}, with loading of around 10% wt. or lower. Studies have demonstrated that the perimeter sites at the WO_3–Al_2O_3 interface, stabilized by Al–O–W bonds, are the primary active sites for selective 1,3-PD production. Maximizing the density of such interfacial sites is therefore a key design criterion for selective catalysts [6–8].

It has been suggested that a larger number of oxygen defects in WO_3 enhances the 1,3-PD yield in glycerol hydrogenolysis. J. Wang et al. studied this phenomenon by preparing a series of mesoporous Pt-WOx catalysts, where the one with the most oxygen vacancies showed the highest 1,3-PD selectivity (18% glycerol conversion with 39.2% 1,3-PD selectivity) [12]. Y. Niu et al. developed two catalysts with high and low quantities of oxygen vacancies (Pt/H-WO_3 and Pt/L-WO_3, respectively) and found an increase in 1,3-PD conversion and selectivity, namely up to 63.8% glycerol conversion and 43.2% selectivity for 1,3-PDO, for the Pt/H-WO_3 catalyst [13].

The loading of WO_3 over the catalyst has also been studied to assess the optimal amount to maximize the 1,3-PD yield. S. García-Fernández et al. studied the effect of the WO_3 surface density over different Pt/WO_3 loadings and discovered a maximum in 1,3-PD selectivity (54% with 9% wt. Pt loading and 26% with 2% wt. Pt loading) at 2.2 W atoms nm^{-2} surface density [5]. T. Aihara et al. further investigated the ideal amount

of WO_3 loading in the catalyst, finding that 7% in weight of WO_3 gave the highest 1,3-PD selectivity (24% yield), with a W/Al (atom/atom) ratio of 0.04 [14]. N. Lei et al. recently tested the optimal WO_3 loading over a wide range (from 5% wt. to 40% wt.), finding 48% selectivity for 1,3-PD as optimal with 10% wt. WO_3 loading [10].

Since both the surface density and the crystallographic structure of WO_3 critically determine catalytic performance, we hypothesized that pre-synthesized WO_3 nanosheets, produced by an innovative fast hydrothermal methodology that we developed, could serve as a strategy to introduce crystalline monoclinic WO_3 at moderate loading (10% wt.), while simultaneously providing a 2D morphology that maximizes the fraction of perimeter sites relative to isotropic particles of equivalent dimensions [7]. This approach explicitly decouples crystallinity from loading, which cannot be resolved by conventional wet impregnation, where crystalline WO_3 formation only appears at high loadings (>20%) [10,15]. Such a method simultaneously generates 3D aggregates with reduced perimeter/volume ratios as there is no control over the particles' shape [5,16]. By controlling the nanosheet dimensions and crystallite size during synthesis, we aimed to isolate the effect of the WO_3 crystalline phase on glycerol hydrogenolysis activity and selectivity, independently of loading effects.

The properties of WO_3 nanosheets depend on the synthesis route used to obtain them; thus, a new, fast hydrothermal synthesis method and its optimization are proposed in our paper to obtain the optimal properties for our glycerol hydrogenolysis reaction in terms of nanosheet dimensions and WO_3 crystallite size.

Such modified hydrothermal exfoliation, used to produce our nanosheets, is a one-step process that uses inexpensive and environmentally friendly chemicals as compared to the conditions used in other methods like sol–gel synthesis and chemical vapor deposition.

Normally, an advantage of hydrothermal exfoliation is its easy scalability as it is a one-step process performed in a simple autoclave. Nevertheless, this technique requires relatively severe conditions (temperatures of 120 °C to 160 °C and autogenic pressures) [17], acidic substances such as HCl or HNO_3 [18,19] and long reaction times (12 h to 24 h) [17,18], often with the use of surfactants to improve the particle dimension distribution [19–21]. Table 1 summarizes the experimental conditions from different studies for the preparation of nanosheets. Here, we propose a new approach to producing WO_3 nanosheets that avoids the use of surfactants and reduces the reaction time to 4 h. We also examine the evolution of the crystalline phases during synthesis and precisely measure the particle dimensions and the critical role of citric acid in the final morphology. Finally, we prepare a $Pt/WO_3/Al_2O_3$ catalyst using these nanosheets and compare it with a $Pt/WO_3/Al_2O_3$ one prepared from a literature methodology in a glycerol hydrogenolysis reaction, with loading amounts comparable to the literature (2% wt. Pt and 10% wt. WO_3) [5].

Table 1. Published WO_3 nanosheet synthesis conditions used in hydrothermal methods, with main dimensions when available.

Ref.	Temperature (°C)	Time Required (h)	Diameter (nm)	Thickness (nm)
Yu et al. [17]	160	16	300	40
Han et al. [22]	160	12	155–175	30–35
Ahmed et al. [21]	75	12	150	20–40
Chen et al. [19] *	60	2	83–241	5–10
Zhang et al. [18]	120	24	150	15
Hu et al. [23]	160	24	-	40
Zhang et al. [24]	120	12	60–600	40
He et al. [25]	120	24	100	20
Xiao et al. [26]	160	12	200–300	50
Our work	100	4	109	21

* NaOA and NaOct have been used as surfactants for this synthesis.

2. Results and Discussion

2.1. Nanosheet Synthesis and Morphology

During a typical successful synthesis step (where the nanosheet morphology was obtained), after only one hour of stirring at room temperature, the material appeared mostly amorphous (Figure 1, No Heat). Following the 4 h heating step, the XRD pattern (Figure 1, 4 h) displayed clear peaks corresponding to the orthorhombic phase of tungsten oxide hydrate, $WO_3 \cdot H_2O$, which were retained after calcination (Figure 1, Calcined).

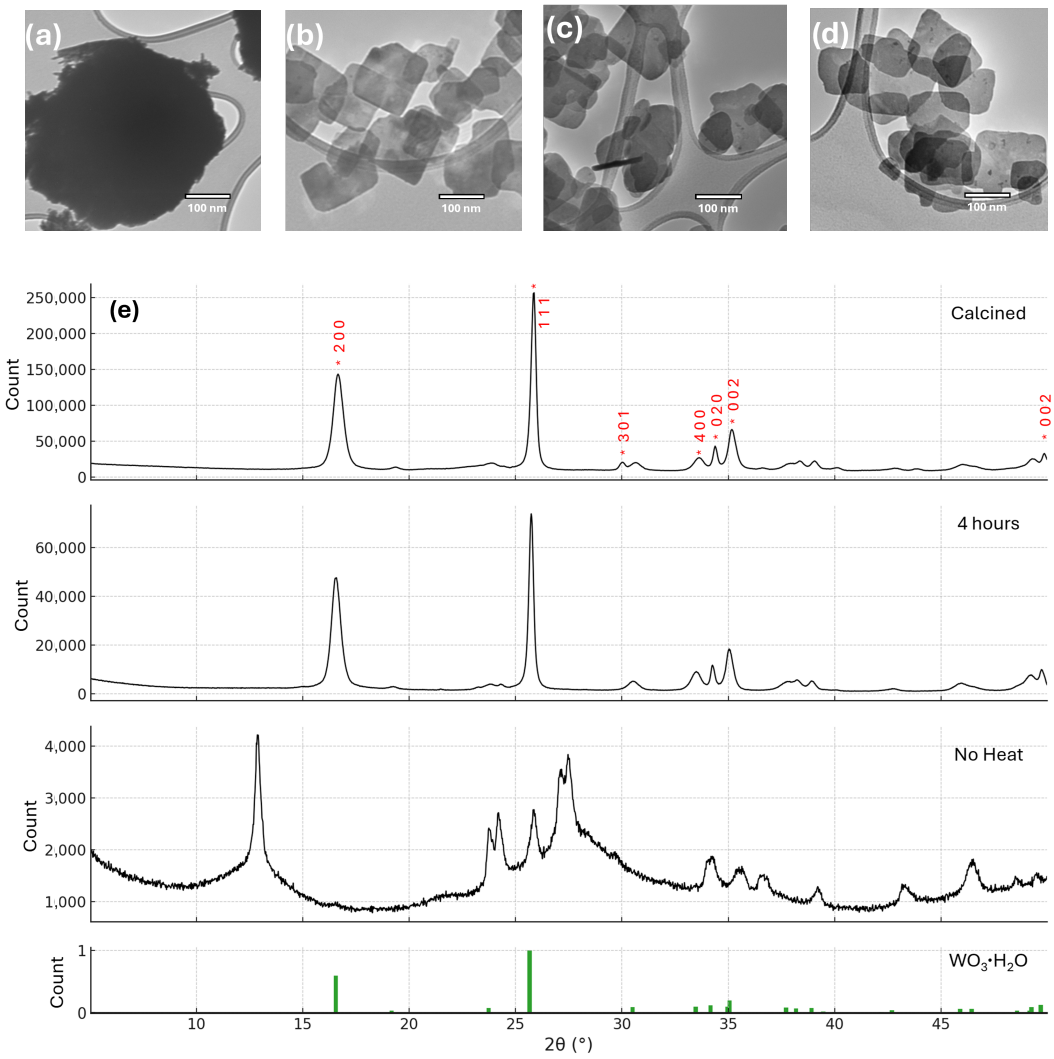


Figure 1. TEM of nanosheets resulting from NS13 with no citric acid (**a**) and NS14 with 1 h of stirring but no heating phase (**b**), after 4 h of heating (**c**) and after reduction in N_2 (**d**). Below (**e**), comparison of XRD results for each obtained nanosheet sample, with the reference of $WO_3 \cdot H_2O$ at the bottom.

This phase belongs to space group *P n m b* (no. 62), with lattice parameters $a = 1.07$ nm, $b = 0.52$ nm and $c = 0.51$ nm. Characteristic peaks were observed at 17° for (200) and 26° for (111), with the typical $WO_3 \cdot H_2O$ peaks from 33° to 36°, including (400), (020) and (002) (Figure 1, Calcined).

During the heating phase, the solid was exfoliated to nanosheets and grew the proper crystal phase over time (Figure 1, No Heat and 4 h). To better prove our hypothesis, an experiment was performed while sampling over 6 h of heating (using NS14 parameters) (Figure 2).

The crystallite size increased over time, reaching a maximum of around 32 nm. Compared to other synthesis routes from the literature for tungsten oxide nanoparticles (sput-

tering or dry ball milling), the crystallite size obtained was larger [27,28]. Concerning hydrothermal synthesis, Hatel et al. [29] performed a 72 h reaction and 5 h of calcination and obtained crystallite sizes of 21 nm to 29 nm. The only work that we could find that obtained a larger crystallite size at a comparable synthesis time was the paper published by Karimkhah et al. [30], where the authors performed liquid-phase deposition for 8 h, obtaining crystallites of 91 nm. However, their synthesis did not result in nanosheets but in nanoflakes. We are not aware of any reports specifically describing crystallite sizes for nanosheet synthesis.

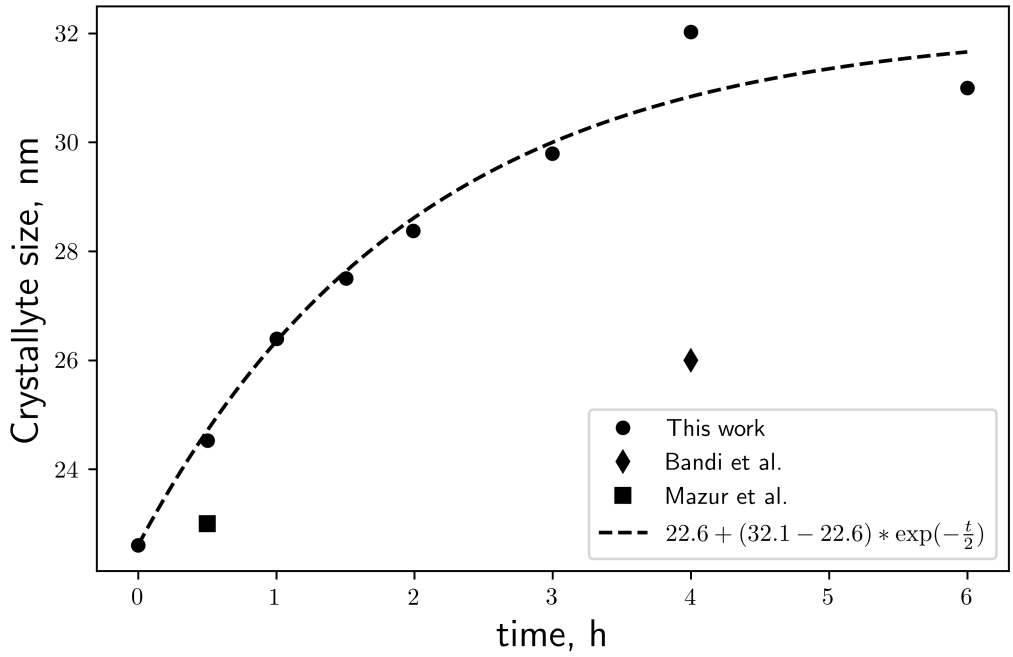


Figure 2. Evolution of the crystallite size of WO_3 nanosheets during synthesis. Scherrer crystallite size increases via a first-order reaction with characteristic constant $2\,h^{-1}$ (dotted line). Comparison between literature data for ball mill synthesis (diamond, Bandi et al. [27]) and a sputtering technique (square, Mazur et al. [28]).

Our proposed synthesis method is therefore able to tune the crystallite size from 22.5 nm to 32 nm.

By interpolating our data, we obtained an equation to calculate the time needed (t) to obtain a target crystallite size (S_{target}):

$$t(\mathrm{h}) = 2 \cdot \ln\left(\frac{9.5}{S_{target}(\mathrm{nm}) - 22.5}\right) \quad (1)$$

The monoclinic crystal phase of $WO_3 \cdot H_2O$ was further confirmed by the diffractogram obtained from the HRTEM images (Figure 3, right).

The image shows a square lattice oriented in the (010) direction, rotated by 45°. Visible planes include (002) at the corners and (–101) on the sides, with external points indicating the (200), (111) and (220) planes. Toward the nanosheet interior, a local rotation of the crystal planes introduces disorder (Figure 3, left).

Sharp diffraction peaks indicate a well-ordered orthorhombic phase, further supporting the hypothesis that citric acid promotes not only exfoliation but also crystallization under these mild hydrothermal conditions. By contrast, the test conducted without citric acid resulted in the formation of large, irregular WO_3 particles with no discernible nanosheet morphology (Figure 1a). In this case, the particles were more spherical and of a much larger average diameter (>300 nm).

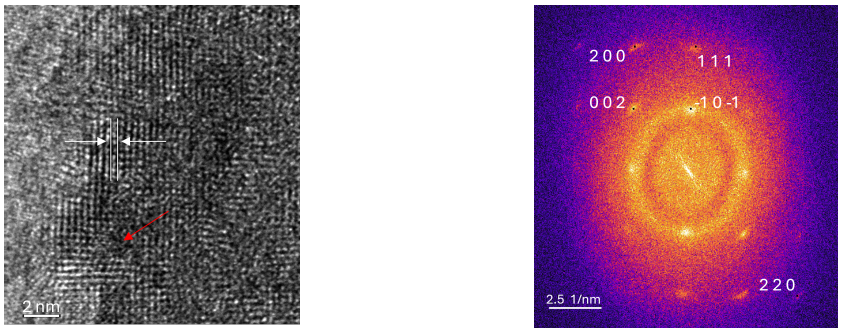


Figure 3. Right: HRTEM image of a single nanosheet. White arrow points to an array of tungsten atoms that we used to confirm the lattice parameter calculation. Red arrow points to a non-crystalline region of the nanosheet. **Left**: Diffractogram obtained from the HRTEM image.

Citric acid acts therefore as a molecular template (like a surfactant) or coordinating ligand and helps to control nucleation and avoid uncontrolled crystal growth. These findings confirm the fundamental role of citric acid in modulating both the morphology and crystallinity of the final product.

Kong et al. [31] studied the role of oxalic acid in WO_3 nanosheet synthesis. We conclude that citric acid has the same coordinating role, i.e., it coordinates with tungsten oxide hydroxyl groups and stabilizes it in nanosheet form.

The literature reports the use of glucose for the synthesis of 2D oxides via dry ball milling synthesis, as well as a few other hydrothermal routes regarding WO_3 nanosheets [18,25,32]. These works never discuss the role of glucose or its influence on the nanosheet size. From NS1 and NS2, in which we kept all parameters constant while adding or completely removing glucose, we obtained, in both cases, nanosheets that were similar in size (see Figure S3a,c in Supplementary Materials). We therefore conclude that glucose has an ancillary role and propose a mechanism of WO_3 exfoliation that does not involve glucose (Figure 4).

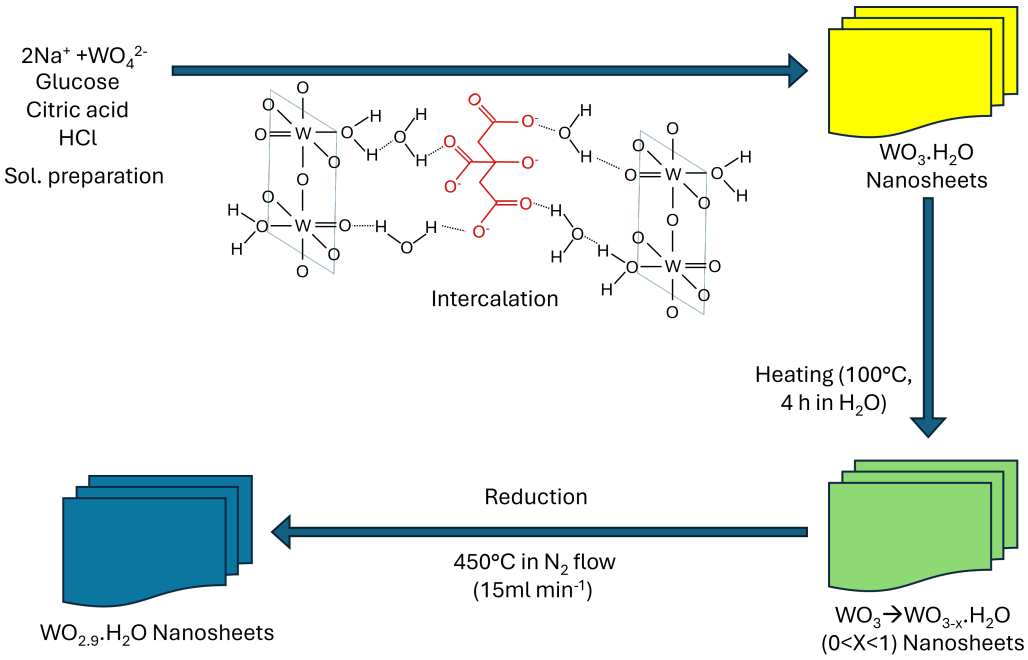


Figure 4. Proposed mechanism of H_2WO_4 nanosheet production [31].

Citric acid plays a key role by coordinating with the $WO_3 \cdot H_2O$ lattice via –OH groups. This influence is also reflected in the nanosheets' shape: the edges become increasingly rounded as the citric acid levels deviate from the optimal value (NS14), as seen in (Figure 5).

Citric acid is therefore the critical factor for the successful formation of nanosheets. Its role as a coordinating agent appears to be essential in directing the morphology of the resulting WO_3 structures. In particular, NS14 yielded the smallest and thinnest nanosheets (Figure 1b–d). The crystalline nature of the resulting $WO_3 \cdot H_2O$ was confirmed by the XRD analysis, as shown in Figure 1e.

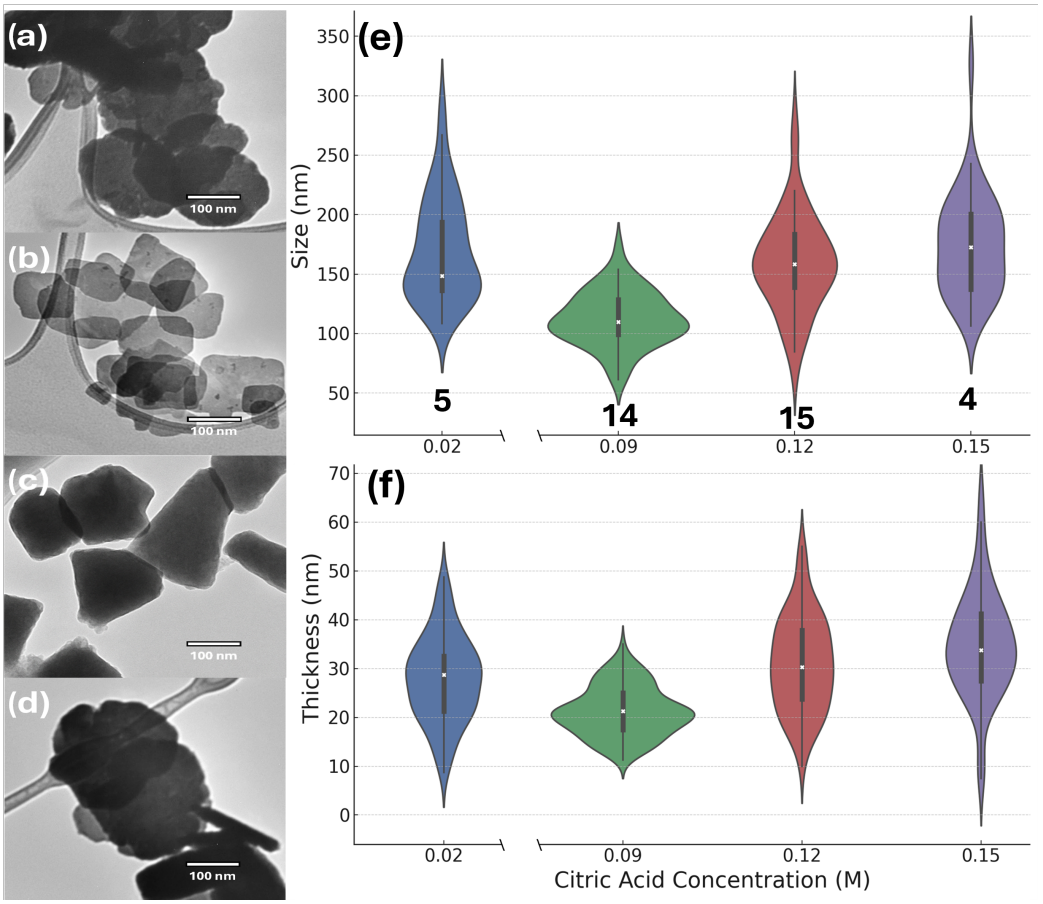


Figure 5. TEM images of NS5, NS14, NS15 and NS4 ((**a**), (**b**), (**c**), (**d**), respectively) and dimensions (**e**) and thickness distributions (**f**). The distributions shown represent the mean square average diameter (*MSA*).

2.2. Nanosheet Dimensions and Thickness

The TEM images illustrate the typical morphologies of the samples obtained in NS4, NS5, NS14 and NS15. Each image displays a small cluster of nanosheets representative of the entire sample (Figure 5).

In NS5, where the amount of the WO_3 precursor is 1.5 times the amount of citric acid (Figure 5e—top), the average *MSA* reaches 148 nm, with diameters from 108 nm to 289 nm. As the citric acid concentration is increased, while keeping the tungsten precursor concentration constant, both the average size and the distribution range narrow.

The smallest *MSA* is observed in NS14, with an average diameter of 109 nm and a tighter distribution (minimum value: 61 nm, maximum value: 172 nm). However, a further increase in citric acid leads to an increment in the dimensions: NS15 shows a median value of 158 nm within a broader range (minimum value: 64 nm, maximum value: 158 nm). This trend is confirmed by NS4, in which we used an even higher citric acid concentration compared to NS15.

This trend is expected: lower citric acid concentrations reduce the likelihood of intercalation between crystal planes, leading to larger, less controlled growth. On the other

hand, excessive citric acid can also destabilize the process, broadening the distribution due to excessive intercalation (Figure 4).

The experiment with NS14 was also repeated with varied dilution in NS7 and NS8, keeping the molar ratios of citric acid and glucose constant. Although the average diameter only slightly changed with the dilution or concentration, a clear difference in nanosheet morphology was observed at higher concentrations, particularly more rounded shapes in NS8 (see Supplementary Materials, Figure S3k,m).

The thickness distribution data, shown in (Figure 5e—bottom) and calculated via Equation (6), indicate that a 1:1.7 molar ratio of $Na_2WO_4 \cdot 2H_2O$ to citric acid provides the thinnest nanosheets. NS14 yielded an average thickness of 21 nm.

Both decreasing and increasing the citric acid concentration resulted in a higher average thickness and broader distributions. In NS5, reduced citric acid gave a thickness from 9 nm to 49 nm, with an average of 29 nm. In NS15, increased citric acid raised the average to 30 nm with a thickness range of 10 nm to 55 nm, and an even further increase in citric acid (NS4) led to an average of 34 nm, ranging from 6 nm to 66 nm. This supports the hypothesis that a citric acid concentration of 90 mmol L^{-1} is required for the best control over the nanosheet thickness.

For further characterization of the nanosheets, see the Supplementary Materials.

Based on the TEM and EELS results, the nanosheets from NS14 (average thickness 21 nm, *MSA* 109 nm) and NS4 (average thickness 34 nm, *MSA* 173 nm) were selected as the WO_3 precursors for catalyst preparation, as they represented the thinnest and thickest nanosheets obtained, respectively, enabling a systematic assessment of the nanosheet dimensions' effects on catalytic performance.

2.3. Pt/WO_3/Al_2O_3 Catalyst Morphology

XRD patterns of the catalysts were obtained for both NN14 and WI (Figure 6). They were then analyzed to observe the phases present in the $Pt/WO_3/Al_2O_3$ catalysts. These XRD patterns were taken on the pre-reduced catalyst (as reaction conditions).

For both catalysts, we can observe the presence of γ-Al_2O_3 from the peaks at 37°, 46° and 67°, which can be identified with the characteristic peaks of the cubic Fd-3m γ-Al_2O_3. It is also possible to observe the presence of Pt in the peak at 39°, which corresponds to the platinum (111) facet of the cubic FCC Fm-3m structure. We evaluated the Pt particle size via the Scherrer equation over the peak at 39.7° (representing the Pt (111) facet). The peak in WI has an FWHM of 0.18°, being much smaller than the peak in NN14, with an FWHM of 0.47°. As the other parameters for the Scherrer equation are the same (K is the shape factor (0.9), λ is the X-ray wavelength (0.15406 nm), β is the full width at half maximum (FWHM) and θ is the Bragg angle (0.2246 rad, corresponding to the (111) plane), we calculated that the average particle size in WI was ca. 52 nm, while, in NN14, it was ca. 18 nm. These values show that Pt is better dispersed on the NN14 nanosheets with respect to the WI catalyst. The key distinction between the catalysts emerges in the NN14 sample, where monoclinic WO_3 diffraction peaks are clearly present. These peaks are absent in the WI catalyst. This observation is particularly significant: at WO_3 loadings below 10% wt, conventional impregnation methods typically produce small WO_3 species in the form of either isolated monotungstates or oligomeric polytungstates, which lack crystalline qualities detectable by XRD [5,16]. The appearance of monoclinic WO_3 in NN14 at equivalent loading (9.5% wt.) directly demonstrates that pre-synthesized nanosheets enable the introduction of crystalline WO_3 phases that are inaccessible through standard impregnation. The WI catalyst, as confirmed by the literature data, does not have any observable peak for crystalline WO_3 with our loading, producing small particles without a

proper crystal structure due to the small dimensions and the impregnation technique used to produce them [5,10,11].

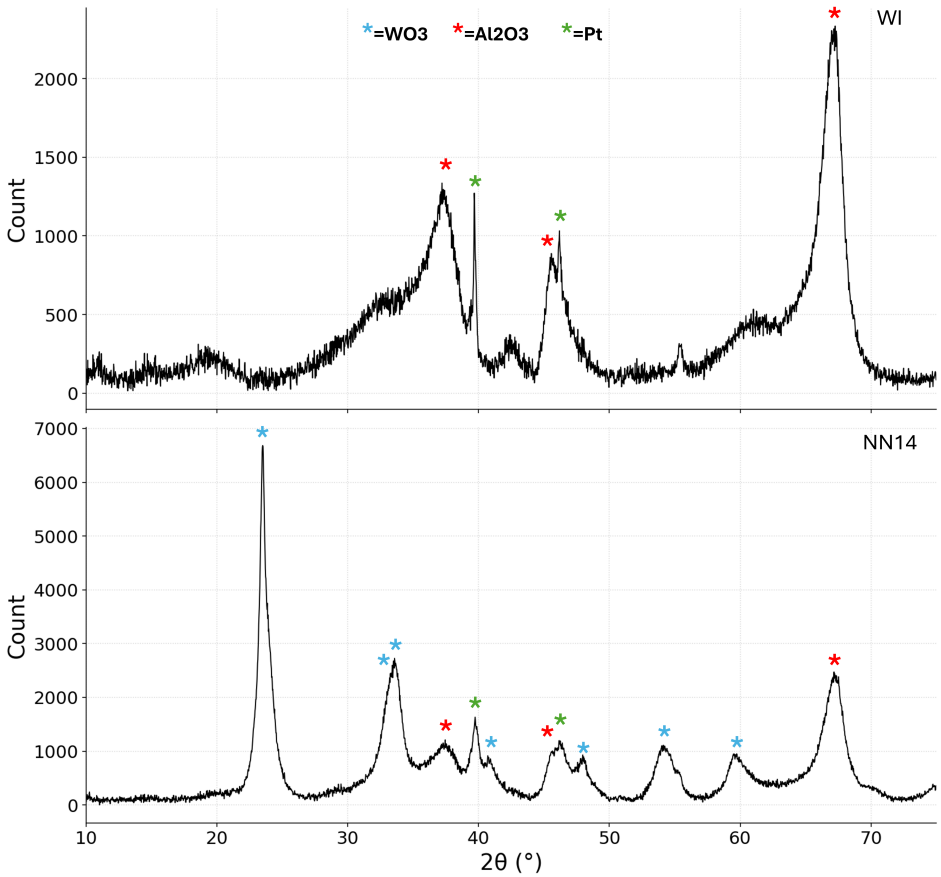


Figure 6. XRD patterns of the WI (**top**) and NN14 (**bottom**) catalysts after 500 °C calcination and pre-reduction. Asterisks indicate diffraction peaks attributed to γ-Al_2O_3 (red), Pt (green) and monoclinic WO_3 (blue, NN14 only).

Our pre-synthesized nanosheets were fixed onto the support surface as tungstite, as evidenced by the previous XRD (Figure 1). Then, the phase changed over the calcination period, producing monoclinic WO_3 with lattice parameters a = 7.306 Å, b = 7.540 Å, c = 7.692 Å. This is consistent with the literature as it is a stable phase for tungsten up to 750 °C, consistent with 500 °C calcination in air [33]. Moreover, for the peak at 23°, we can see the crystallinity change to 10 nm, calculated using the same equation as used for the nanosheets (Equation (4)). The presence of these peaks at loading of 9.5% wt. is proof that we were able to obtain crystalline WO_3 with low loading and enabled us to compare its reactivity to that of a classical wet impregnation catalyst with the same amount of WO_3.

The SEM-EDS images were obtained on the pre-reduced catalyst (as used in the reaction conditions) and taken to represent the overall catalyst surface.

From the SEM-EDS (Figure 7) analysis, we observe a good distribution for both Pt and WO_3 over the Al_2O_3 surface in the catalysts, although the Pt particles should have been better dispersed on the NN14 catalyst. The WO_3 in the WI catalyst was spread throughout the surface, covering a large part of the surface, as with the Pt. It is challenging to ensure that Pt particles are directly deposited on the WO_3 surface, ensuring contact between the two. It could be possible to have Pt in contact with the Al_2O_3 surface instead, possibly leading to side reactions due to Al_2O_3's proximity and its acidity. In the case of the NN14 catalysts, we could observe in the image a general increase in the Pt concentration over the surface, in the same areas as WO_3. This would be a logical consequence of the catalyst

preparation procedure, which allows us to ensure the deposition of Pt over the nanosheets and only afterwards the deposition of the Pt/WO_3 on the support. However, the SEM-EDS images are not sufficient to show a significant difference between the two catalysts, although they show a similar distribution.

The N_2 physisorption results reported in Table 2 show the nanosheets' surface areas, as well as the surface areas of the WI and NN14 catalysts, measured on the pre-reduced catalysts.

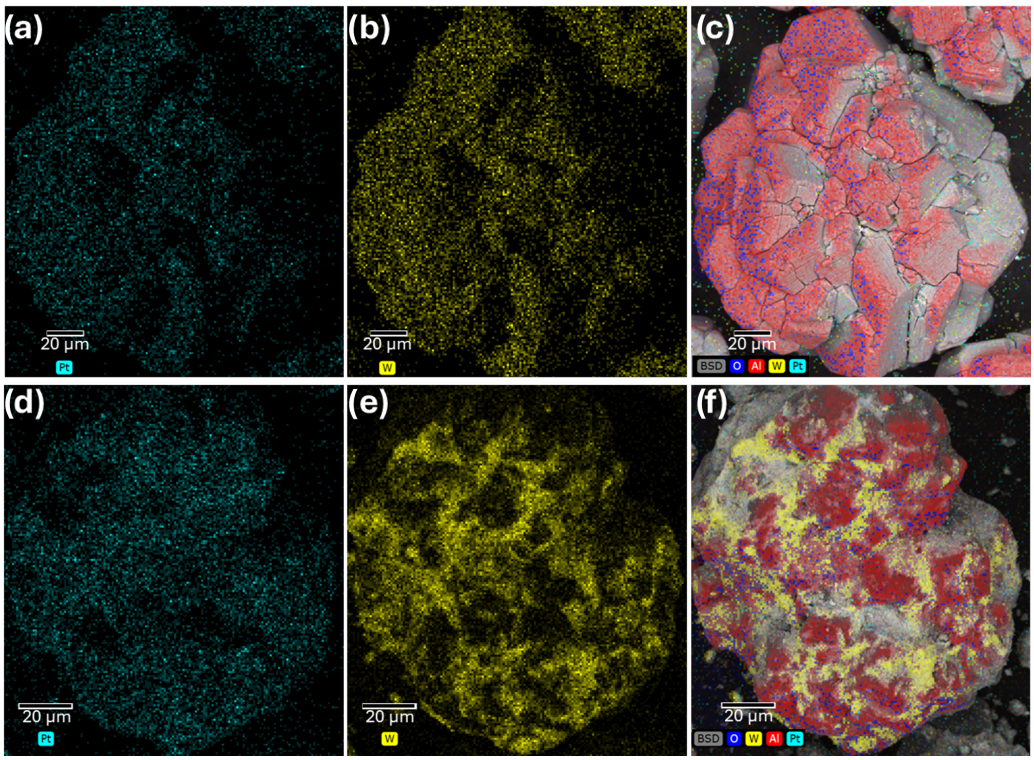


Figure 7. SEM-EDS images of the $Pt/WO_3/Al_2O_3$ WI (**a**–**c**) and NN14 (**d**–**f**) catalysts after 500 °C calcination and three washes with a centrifuge, using 300 mL of Milli-Q water for each wash. Each element is represented by a color: O = blue, W = yellow, Al = red, Pt = cyan.

Table 2. BET analysis results, showing the surface area, pore diameter and total pore volume for the Al_2O_3 precursor, WO_3 nanosheets (NS14) and final catalysts (WI and NN14).

Experiment	Surface Area ($m^2\ g^{-1}$)	Pore Diameter (nm)	Total Pore Volume ($cm^3\ g^{-1}$)
Al_2O_3	205	-	-
NS14	23.5	1.0	0.12
WI	23.8	1.1	0.13
NN14	21.2	1.1	0.08

The nitrogen physisorption results in Table 2 confirm that the surface area differences between the catalysts are negligible: WI and NN14 show 23.8 $m^2\ g^{-1}$ and 21.8 $m^2\ g^{-1}$, respectively—a difference of only 2.7 $m^2\ g^{-1}$. The nanosheets are deposited on the (002) facet (the flat side) of the alumina surface, effectively covering the exposed area without creating additional porosity but decreasing it slightly, as could be observed from the total pore volume difference between WI and NN14 of 0.05 $cm^3\ g^{-1}$. The similar surface area between the catalysts can be attributed to the blockage of Al_2O_3 pores by WO_3 particles and the subsequent calcination, conducted similarly in both the NN14 and WI catalysts.

The XRF composition results reported in Table 3 show the NN14 and WI catalysts' surface compositions. The data reported in Table 3 are further confirmed by the ICP

analysis, which yielded similar results regarding the composition (Table S1). These analyses reveal minimal compositional differences: WI contains 9.6% wt. WO_3 and 2.4% wt. Pt, while NN14 contains 9.5% wt. WO_3 and 1.9% wt. Pt. Based on this, and on the surface area, the resulting W surface densities are $\rho_W = 1.85$ W atoms nm^{-2} for the WI catalyst and $\rho_W = 1.82$ W atoms nm^{-2} for the NN14 catalyst, both within the ranges associated with polytungstate species and optimal 1,3-PDO selectivity in the literature [5,11]. It should be noted that this formula was derived assuming the two-dimensional dispersion of WO_3 species on the support surface. In the case of the NN14 catalyst, where WO_3 is present as crystalline nanosheets of controlled thickness (21 nm), this assumption underestimates the true surface coverage, as a fraction of the W atoms are located in the bulk of the nanosheet and are not surface-exposed. The reported ρ_W value for NN14 should therefore be interpreted as an apparent surface density. This is shown by the SEM-EDS analysis, where the Al_2O_3 surface covered by WO_3 in the NN14 catalyst is slightly larger than the one covered on the WI catalyst.

Table 3. WI and NN14 surface compositions as analyzed by XRF directly on the powder, before the reduction performed prior to each test.

Catalyst	Al_2O_3 (% wt.)	WO_3 (% wt.)	Pt (% wt.)
WI	88.0	9.6	2.4
NN14	88.6	9.5	1.9

The surface acidity of the catalysts was estimated by NH_3-TPD performed on both the WI and NN14 catalysts, and the results are listed in Table 4.

Table 4. WI and NN14 acid sites per gram of catalyst as evaluated by NH_3 desorption.

Catalyst	Weak Acid Sites (μmol g^{-1})	Medium Acid Sites (μmol g^{-1})	Strong Acid Sites (μmol g^{-1})
WI	50.5	16.1	-
NN14	48	38	19.2

As shown in Table 4, the WI catalyst presents only weak and medium acid sites (50.5 μmol g^{-1} and 16.1 μmol g^{-1}, respectively), with no measurable strong acid sites. This is in accordance with the literature, where the acid site distribution of a catalyst prepared by wet impregnation is typically reported to decrease in the order of weak > medium > strong [5]. Such a distribution is usually associated with selectivity toward 1,3-PD and a low propensity for over-hydrogenolysis, a behavior that has been documented for WO_3 loadings below approximately 20% wt. [15]. The Al_2O_3 support was the same for both catalysts and was subjected to the same thermal treatment; its contribution to the acidity baseline was therefore expected to be comparable in the two samples, and, on its own, it is not known to produce strong or markedly different medium acid sites between catalysts. While the absolute acid site concentration may be partially set by this baseline, the focus of the present study is on the relative differences between the two final catalysts, for which a semi-quantitative comparison of the NH_3-TPD profiles is sufficient to argue that the support contribution is secondary to that of the WO_3 phase. The NN14 catalyst, in contrast, exhibits a qualitatively different acidity profile: weak sites (48 μmol g^{-1}) remain comparable to WI, medium sites increase substantially (38 μmol g^{-1}), and an additional contribution of strong acid sites appears at 19.2 μmol g^{-1}. The appearance of these strong acid sites in NN14 is consistent with the crystalline monoclinic WO_3 phase identified by XRD. According to the literature, crystalline WO_3 surfaces are more prone than dispersed monotungstate or isolated polytungstate species to developing strong surface acidity upon H_2 pre-reduction, a process commonly described in terms of the H-spillover-induced transformation of Lewis-

type W centers into Brønsted-type W–OH sites; here, we adopt this picture only as the most widely accepted mechanistic interpretation, without claiming direct Brønsted/Lewis discrimination from our NH_3-TPD data alone [34]. The presence of strong acid sites is in line with the higher surface acidity of the bare nanosheets independently measured through pH_{PZC} (see Figure S2 in the Supporting Information). Strong surface acid sites have, in turn, been reported to promote secondary dehydration steps that lead to the formation of 1-propanol and 2-propanol via over-hydrogenolysis pathways, rather than selective primary C–O bond cleavage to 1,3-PD [15]. The mechanistic picture that emerges is therefore the following: WI and NN14 carry virtually identical WO_3 loadings (9.6% vs. 9.5% wt.) and comparable effective surface densities once the nanosheet thickness is taken into account, yet they display qualitatively different acidity profiles, which we attribute to the difference in WO_3 crystallinity. The amorphous polytungstate-dominated WI lacks strong sites, whereas the crystalline monoclinic phase introduced through the nanosheet route in NN14 brings them in. By decoupling loading from crystallinity through the pre-synthesised nanosheets, the appearance of strong acid sites can be linked here primarily to the crystalline state of the WO_3 phase rather than to its nominal loading.

2.4. Catalytic Test Results

The results of the catalytic tests performed on the WI, NN14 and NN4 catalysts are shown in (Figure 8) in terms of the glycerol reaction rate (left) and selectivity (right), calculated via Equation (2) and Equation (3), respectively. A test with Al_2O_3 was performed as well, leading to no conversion (∼1%), and the results are reported in the Supplementary Materials, Table S3, as well as all reactions' carbon balances, which were considered acceptable. In Figure S5, we also present the yield profiles over the reaction time for 1,3-PD and 1,2-PD. GC analyses of the gas phase were also performed, and these reported negligible CH_4 or CO_2 content. We assumed that the resulting C atoms missing from EG production were probably converted into MeOH, as is typical of similar catalysts. However, HPLC was performed with an RI detector in an aqueous solution. The WI catalyst achieved the highest average glycerol conversion rate (1.23 $mmol_{Gly}\ g_{cat}^{-1}\ h^{-1}$), approximately 3.8 times higher than that of NN14 (0.32 $mmol_{Gly}\ g_{cat}^{-1}\ h^{-1}$) and 20 times higher than that of NN4 (0.06 $mmol_{Gly}\ g_{cat}^{-1}\ h^{-1}$). Meanwhile, the reaction performed with only Al_2O_3 as a blank test brought no appreciable glycerol conversion. This monotonic decrease in the conversion rate with increasing nanosheet thicknesses can be primarily ascribed to the presence of crystalline monoclinic WO_3 in the nanosheet-based catalysts, as evidenced by XRD (Figure 6) and consistent with the NH_3-TPD profiles reported in Table 4. From previous studies, Pt's increased distribution should improve the catalytic performance overall [5,14]. We observed better Pt dispersion in the NN14 catalyst, but the observed average glycerol reaction rate was much higher in the case of WI (1.23 versus 0.32 $mmol_{Gly}\ g_{cat}^{-1}\ h^{-1}$). If the Pt distribution played a major role, we would have obtained the opposite result. According to the literature, Pt's action is effective only if in interaction with the WO_3 support, as proven by DFT and operando studies [8,9]. These studies show that selective C–O cleavage occurs at the Pt–WO_3 perimeter, where H spillover from Pt generates Brønsted W–OH centers. We can therefore concluded that WO_3's crystallinity effect has greater importance than the Pt distribution. Thus, we draw the conclusion that WO_3's crystallinity was responsible for the decreased activity rather than Pt having major effects on the reaction rate.

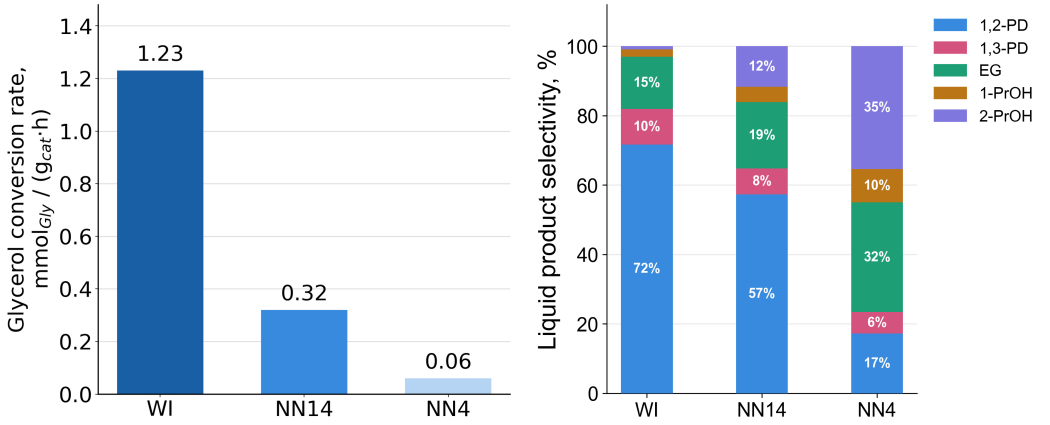


Figure 8. Left: Average glycerol conversion rates of WI, NN14 and NN4 catalysts. **Right**: Liquid product selectivity of WI, NN14 and NN4 catalysts.

We observe a systematic shift toward over-hydrogenolysis products, which would support this interpretation. Moving from WI to NN14 to NN4, the combined selectivity toward 1-propanol and 2-propanol rises from 3% to 16% to 45%, while 1,2-PD selectivity drops from 72% to 57% to 17%. Such a shift toward over-hydrogenolysis products is consistent with the progressive emergence of strong acid sites associated with larger crystalline WO_3 domains. It is worth noting that this trend is observed while both WI and NN14 maintain apparent WO_3 surface densities below the critical threshold of 2.2 W atoms nm^{-2}, which supports the view that the catalytic divergence is driven by the crystalline state of the WO_3 phase rather than by an increase in loading. In fact, the conversion rate drops because NS4 has an average thickness of 34 nm and lateral dimension of 173 nm, i.e., it is 1.6 times thicker and 1.6 times wider than NS14 (21 nm thick and 109 nm). For platelet-like crystals, the perimeter-to-volume ratio scales as 1/d (where d is the lateral diameter), so NN4 has a 1.6 times smaller Pt-WO_3 interfacial perimeter per unit WO_3 mass than NN14, assuming a similar and uniform Pt distribution over the two catalysts. This is consistent with the trends observed: the reaction rate drops further from NN14 (0.32 mmol$_{Gly}$ g$_{cat}^{-1}$ h^{-1}) to NN4 (0.06 mmol$_{Gly}$ g$_{cat}^{-1}$ h^{-1}), and the propanol selectivity rises from 16% to 45% because of the larger nanosheets of crystalline WO_3, which leads to an increase in surface acid sites, responsible for over-hydrogenolysis reactions.

All three catalysts were tested under identical conditions, and both WI and NN14 maintained apparent tungsten surface densities below the critical 2.2 W atoms nm^{-2} threshold. The WO_3 crystalline phase, not the loading or H_2 limitation, is the driving force for the observed differences in secondary product selectivity.

The stability of the catalyst was investigated and more information can be found in the Supplementary Materials (Figures S6–S8). Overall, both catalysts' performance decreased after 48 h of reaction without the presence of relevant carbon deposition on the catalyst. However, the structural integrity of the NN14 catalyst was compromised over the long reaction period, possibly due to the leaching of the WO_3.

3. Materials and Methods

3.1. Reagents

Sodium tungstate dihydrate ($Na_2WO_4 \cdot 2H_2O$, 99+% purity) was acquired from Thermo Scientific, Canada Ltd. (Mississauga, ON, Canada) and used as a precursor. Glycerol (99.0% purity), ammonium metatungstate hydrate (>85% WO_3 basis), hexachloroplatinic acid hexahydrate (40% Pt), γ-Al_2O_3 40-mesh powder (99.99% purity), anhydrous citric acid (99.5% purity), D-glucose (99+% purity) and hydrochloric acid (36.5–38%) were purchased

from Fisher Chemical, Canada Ltd. (Ottawa, ON, Canada). All chemicals were used without further purification.

3.2. Nanosheet Synthesis

The nanosheets were prepared in a 250 mL two-necked flask, where 80 mL of Milli-Q water was added. A thermometer, mounted on a side neck, measured the temperature of the reacting mixture. A bubble condenser was equipped on the central neck, with cooling water at 15 °C.

While stirring vigorously at 600 rpm, 4 mmol of $Na_2WO_4 \cdot 2H_2O$ was added. Complete dissolution was achieved over 5 min. Then, 7.2 mmol of citric acid and 20 mmol of D-glucose were added consecutively (see Table 5 for each quantity in detail). After all components had fully dissolved, 4 mL of HCl (6 M) was added dropwise in one minute. The solution was then stirred continuously at room temperature for 1 h. During the first 10 min to 15 min, the solution turned from transparent to pale yellow and finally yellow, indicating the onset of WO_3 particle precipitation (the sample of the precipitate taken at this time is referred to as "No Heat").

The flask was then heated to 100 °C and maintained under stirring at 600 rpm for 4 h. During this phase, the solution gradually changed from yellow to green, signaling exfoliation and phase transition. The reaction mixture was then allowed to cool (the sample of the precipitate taken at this time is referred to as "4 h").

The resulting nanosheets were separated by centrifugation (Beckman Avanti J-20 XP, Beckman Coulter, Inc., Brea, CA, USA) at 1300 rpm for 15 min, followed by two washes with 100 mL Milli-Q water and two washes with 50 mL of dry EtOH, with each wash followed by another centrifugation step under the same conditions. The resulting nanosheets were calcined at 350 °C for 2 h in a tubular furnace with an air flow at 15 mL min^{-1} to reduce the residual chlorine content. The thus-produced nanosheets appeared as a green–yellow powder (the sample of the precipitate taken at this time is referred to as "4 h"). Each experiment led to nanosheets, and they are named NSX, where X is the test number.

We varied the concentration of each reactant to evaluate their effects on the morphology, as seen in Table 5, yielding 12 experiments in water. Two extra experiments were carried out in methanol (NS11) and ethanol (NS10) to study the effects of the reaction temperature and solvent.

Table 5. Experimental parameters used for WO_3 nanosheet synthesis. Additional tests (NS6, NS9, NS10, NS11, NS12 and NS13) resulted in amorphous nanoparticles with no specific shape. Solvents for tests NS10 and NS11 are given in parentheses.

Sample	ST (M)	CA (M)	Glu (M)	HCl (mL)	d (nm)	t (nm)
NS1	0.05	0.07	-	4	127	-
NS3	0.05	0.07	0.12	4	119	-
NS4	0.05	0.15	0.25	4	172	34
NS5	0.05	0.02	0.25	4	148	29
NS7	0.03	0.04	0.12	4	132	-
NS8	0.08	0.11	0.38	4	120	-
NS14	0.05	0.09	0.25	4	109	21
NS15	0.05	0.12	0.25	4	158	30
NS6	0.05	0.15	0.12	4	-	-
NS9	0.05	0.07	0.25	0.4	-	-
NS10 (EtOH)	0.05	0.07	0.25	-	-	-
NS11 (MeOH)	0.05	0.07	0.25	-	-	-
NS12	0.12	0.13	0.13	1.67	-	-
NS13	0.05	-	0.25	4	-	-

ST = sodium tungstate; CA = citric acid; Glu = glucose; d = average diameter; t = thickness.

3.3. $Pt/WO_3/Al_2O_3$ Catalyst Synthesis

The $Pt/WO_3/Al_2O_3$ catalysts were prepared by wet impregnation. The literature catalyst (WI) was prepared by subsequent wet impregnation as described by S. G. Fernandez [5]. First, 0.8637 g of ammonium tungstate was dissolved in 3.3 mL of Milli-Q water. The solution was then added dropwise in 30 s to 6.7 g of Al_2O_3 while stirring. The wet powder was left to dry under a vent and then it was calcined at 500 °C for 2 h with a temperature ramp of 3 °C min^{-1} and an air flow at 50 mL min^{-1}. Afterwards, 0.4 g of $H_2PtCl_6 \cdot 6H_2O$ was dissolved in 3.3 mL of water and the solution was then added dropwise in 30 s to the WO_3/Al_2O_3 catalyst while stirring. The powder was left to dry under a vent and then calcined at 500 °C for 2 h with a temperature ramp of 3 °C min^{-1} and an air flow at 50 mL min^{-1}. The calcination was performed at 500 °C in dry air to avoid any residual chloride on the catalyst.

The nanosheet catalysts obtained from the usage of nanosheets NS14 and NS4 (producing catalysts NN14 and NN4, respectively, when attached to Pt and Al_2O_3) were prepared in a similar way by solving 0.4 g of $H_2PtCl_6 \cdot 6H_2O$ in 1.5 mL Milli-Q water and adding it dropwise to 0.75 g of the previously produced nanosheets while stirring. NS14 had an average thickness of 21 nm, while the mean square average diameter (*MSA*) was 109 nm. NS4 had an average thickness of 34 nm, while the *MSA* was 173 nm. These values were calculated through TEM and EELS analyses.

The powder was left to dry and then mixed with 3.5 mL of Milli-Q water and sonicated for 15 min to finally add this solution to 6.9 g of Al_2O_3 while stirring. The catalyst was left to dry and then calcined at 500 °C for 2 h with a temperature ramp of 3 °C min^{-1} and an air flow at 150 mL min^{-1}.

Before the experiment, both catalysts were pre-reduced in a tubular furnace with a flow of 5 mL of H_2 and 45 mL of N_2 flow at 250 °C for 90 min, with a temperature ramp of 3 °C min^{-1}.

3.4. Glycerol Hydrogenolysis Catalytic Tests

The catalytic tests were performed in a Parr autoclave of 1 L equipped with a pressure gauge and impeller and further modified with a sampling valve. In this setup, 400 mL of glycerol aqueous solution at 2.5% wt. was poured in, followed by 1.5 g of catalyst. Then, two purging steps were performed: in the first one, Ar was flushed through the reactor for 10 min to purge the air; in the second one, H_2 was flushed through the reactor for 5 min to purge the Ar. Finally, H_2 was fed to the reactor up to 2800 kPa and it was heated to 200 °C, reaching an operating pressure of 5000 kPa while stirring at 1500 rpm. The reaction was kept in such conditions for 5 h while sampling the solution each hour. After such time, the reactor was quenched with a bucket of water and ice until it reached 23 °C, and a gas sample was analyzed through a GC device equipped with a TCD detector, while the collected liquid samples were analyzed through an HPLC instrument equipped with an Aminex HPX-87H (Bio-Rad Laboratories, Hercules, CA, USA) and an RI detector.

The glycerol concentration was selected as 2.5% because diluted feeds minimize diffusional effects in batch reactors and to better compare the results with those of similar literature studies [6].

The final glycerol reaction rate and selectivity over the liquid products were calculated using the following equations:

$$Average\ glycerol\ conversion\ rate = \frac{mmol_{Gly,\,reacted}}{g_{cat} \cdot h} \quad (2)$$

$$Selectivity_i = \frac{mol_i}{\sum_j mol_j} \times 100 \quad (3)$$

where *i* is the considered species, while *j* is any liquid product.

3.5. Characterization

A Hitachi H-7500 transmission electron microscope (TEM) (Hitachi, Tokyo, Japan) operating at 120 kV imaged the samples, with the electron energy set at 80 kV. Samples were prepared on lacey copper grids (Electron Microscopy Sciences (Morgantown, PA, USA), 300 mesh, 50 micron) after elution in 5 mL of EtOH and sonication for 30 min.

HRTEM images of the nanosheets were obtained using a Talos F200X G2 (Thermo Fisher Scientific, Waltham, MA, USA) operated at 200 keV after elution in 5 mL of EtOH and sonication for 30 min.

Powder XRD measurements were carried out using a Panalytical X'Pert Pro (Malvern Panalytical, Malvern, UK) MPD diffractometer operating at 40 kV and 50 mA, equipped with a Cu Kα radiation source (wavelength of 1.5406 Å).

Powder XRD analyses were performed from 5° to 90° to assess the crystallinity of the nanosheets using Scherrer's equation; see Equation (4). To monitor the evolution of their crystal dimensions, nanosheet samples were collected before and during the heating phase and thermal treatment (see Figure 2). The crystallite size was estimated as well by Equation (4):

$$D = \frac{K\lambda}{\beta \cos\theta} \tag{4}$$

where D is the crystallite size, K is the shape factor (0.9), λ is the X-ray wavelength (0.15406 nm), β is the full width at half maximum (FWHM) and θ is the Bragg angle (0.2246 rad, corresponding to the (111) plane).

To evaluate the $Pt/WO_3/Al_2O_3$ catalysts (WI and NN14), the analyses were carried out from 10° to 75° to observe the different crystal phases in the catalysts, and the crystallinity was evaluated at the peak at θ = 0.2007 rad.

SEM-EDS analyses of the $Pt/WO_3/Al_2O_3$ catalysts were performed using a Thermo Fisher Phenom XL G1 with a 15 kV source and 10 Pa vacuum.

Particle size distributions were obtained by treating the TEM images with the ImageJ software (ImageJ 1.54g in Java 1.8.0-345). For each image, the software recorded all minimum and maximum Feret diameters across all nanosheet populations.

We then calculated the *MSA* between the minimum and maximum Feret diameters (d_{min} and D_{max}, respectively; see Equation (5)):

$$MSA = \sqrt{\frac{1}{2}\left(d_{min}^2 + D_{max}^2\right)} \tag{5}$$

The specific surface area and porosity of the nanosheets were determined via N_2 adsorption/desorption isotherms at −196 °C, using a Micromeritics Tristar II 3020 (Micromeritics Instrument Corporation, Norcross, GA, USA) and applying the Brunauer–Emmett–Teller (BET) and Barrett–Joyner–Halenda (BJH) models, respectively. Samples were pre-treated at 150 °C for 4 h under a constant N_2 flow before analysis.

Temperature desorption analyses of ammonia (NH_3-TPD) were performed with a Microtract Belcat II instrument (Microtrac, Osaka, Japan). The samples were treated at 150 °C for 1 h under a He flow (30 mL min^{-1}); next, the temperature was reduced to 100 °C and 10% vol. NH_3/He (30 mL min^{-1}) was flown for 40 min, followed by purging with pure He (30 mL min^{-1}) for an hour always at 100 °C. Finally, the analysis was performed by ramping up the temperature (10 °C min^{-1}) to 500 °C under the same He flow. Peaks were identified as weak (150 °C–200 °C), medium (200 °C–350 °C) or strong (350 °C–500 °C).

Electron energy loss spectroscopy (EELS) measurements were conducted for thickness evaluation using a Talos F200X G2 operated in STEM mode at 200 keV. An ENFINIUM ER

977 dual-EELS camera (Gatan, Inc., Pleasanton, CA, USA) was used with a 60 mm camera length, a 100 µm C2 aperture and a collection angle of 3.26 mrad. The absolute thickness t was calculated from the definition of λ, given in Equation (6) [35]:

$$\lambda = \frac{106F\frac{E_0}{E_m}}{\ln(2\alpha\frac{E_0}{E_m})} \quad (6)$$

where $F = 0.618$ is the relativistic factor, E_0 = 200 keV is the electron beam intensity, $\alpha = 3.26$ mrad is the collection semi-angle and E_m is the average energy loss, expressed in eV.

The multiple atomic number Z in WO_3 was used to calculate E_m (Equation (7)). We considered the atomic number 1/4 W and 3/4 O in Equation (8).

$$E_m = 7.6Z^{0.36} \quad (7)$$

$$Z = \frac{\sum_i f_i Z_i^{1.3}}{\sum_i f_i Z_i^{0.3}} \quad (8)$$

We performed this analysis on the most different samples among the nanosheet experiments: NS4, NS5, NS14 and NS15.

To further evaluate the nanosheets' properties, the band gap and pH_{PZC} were evaluated and are reported in the Supplementary Materials (Figures S1 and S2).

X-ray fluorescence (XRF) analyses were performed using a Bruker S2 PUMA Series 2 energy-dispersive spectrometer (EDXRF) (Bruker, Billerica, MA, USA), equipped with a 50 W long-life X-ray tube and a HighSense™ silicon detector. Elemental compositions were determined using the SPECTRA.ELEMENTS software suite (software version 3, Bruker) with the SMART-QUANT FP module operating in full Fundamental Parameters (FP) mode, which requires no external calibration standards. The XRF analysis was confirmed by ICP analysis, as further described in the Supplementary Materials (Table S1).

The HPLC analyses performed on the glycerol hydrogenolysis samples used an Agilent 1260 Infinity II (Agilent Technologies, Santa Clara, CA, USA) equipped with an Aminex HPX-87H column with a 0.005 M solution of H_2SO_4 as the eluent and with a flow rate of 0.5 mL min^{-1}.

The $Pt/WO_3/Al_2O_3$ catalysts characterized were WI and NN14, which were studied to assess the different results between the two synthesis methods.

The surface density ρ_W W nm^{-2} was calculated using the formula from S. Fernandez et al., shown in Equation (9), considering the results obtained from XRF to better compare the literature to our results [5].

$$\rho_W\left[\frac{\text{W atoms}}{\text{nm}^2}\right] = \frac{\frac{x_W}{M_W}\cdot N_A}{SA_{Al_2O_3}\cdot(1-(x_{WO_3}+x_{PtO}))} \quad (9)$$

where x_W is the mass fraction of the W species in the $Pt/WO_3/Al_2O_3$ catalyst; M_W is the atomic weight of tungsten; N_A is the Avogadro number; $SA_{Al_2O_3}$ is the surface area of the alumina before impregnation (from Fisher chemical analysis), expressed in $nm^2\ g^{-1}$; x_{WO_3} is the mass fraction of the tungstate oxide; and x_{PtO} is the mass fraction of the platinum oxide. We considered all W and Pt in the catalyst as WO_3 and PtO, since the XRF analysis was performed after calcination in air, without pre-reduction.

4. Conclusions

WO_3 nanosheets synthesized via the fast hydrothermal method enabled the introduction of crystalline monoclinic WO_3 at 9.5% wt. loading in $Pt/WO_3/Al_2O_3$ catalysts, which has

never been tested with conventional wet impregnation, where only by exceeding 12% wt. was a change in crystallinity observable [10]. The process demonstrates a 50–80% reduction in synthesis time compared to existing hydrothermal routes [17,22] while producing nanosheets with controlled dimensions (average diameter 109 nm, thickness 21 nm) and a defined monoclinic crystalline phase. Citric acid emerged as the critical parameter governing the nanosheet morphology and crystallinity through its role as a chelating ligand via hydroxyl groups.

The catalytic investigation of glycerol hydrogenolysis reveals a counterintuitive finding: crystalline monoclinic WO_3 at low loading suppresses the conversion rates and shifts selectivity toward undesired over-hydrogenolysis products (1-propanol and 2-propanol). The conversion rate decreased from 1.23 $mmol_{Gly}\ g_{cat}^{-1}\ h^{-1}$ with amorphous WO_3 species to 0.32 $mmol_{Gly}\ g_{cat}^{-1}\ h^{-1}$ with crystalline WO_3, despite maintaining WO_3 surface densities below the literature optimum of 2.2 W atoms nm^{-2}. We concluded that, under the controlled conditions of equal nominal WO_3 loading (9.5–9.6% wt.) and an equal effective W surface density, the WO_3 crystalline phase is the dominant variable governing the observed catalytic divergence between WI and NN14. More importantly, the results show that the amorphous and polytungstate nature of WO_3 in conventional catalysts is actually beneficial for achieving high 1,3-PD selectivity, instead of a limitation to overcome.

These findings redirect the rational design of selective glycerol hydrogenolysis catalysts: future optimization should prioritize maximizing the dispersed polytungstate coverage and minimizing crystalline WO_3 phases. The nanosheet synthesis platform described here provides a valuable tool for systematically investigating how the crystalline phase influences catalytic outcomes in hydrogenolysis and related reactions. Additionally, the controlled variation of the nanosheet dimensions offers potential for optimizing their performance in other catalytic applications beyond glycerol conversion.

Supplementary Materials: The following supporting information can be downloaded at https://www.mdpi.com/article/10.3390/catal16070604/s1, Figure S1: Tauc plot of nanosheets' band gaps from samples NS-5, NS-14, NS-15 and NS-14; Figure S2: pH_{PZC} of nanosheets before and after the heating phase. Also measured with two different saline systems; Figure S3: TEM results of TEM images of NS-1, NS-3, NS-4, NS-8 and NS-9; Figure S4: XRD patterns of NS-15 with different sampling over time to check the crystallite size changes; Figure S5: Instantaneous 1,2-PD yield (on the left) and 1,3-PD yield (on the right) for the WI, NN14 and NN4 catalysts over the whole reaction period; Figure S6: TGA performed over spent catalysts after 48 h of reaction under the same conditions (50 bar of H2, 200 °C, stirring at 1500 rpm, 400 mL of 2.5% wt. glycerol water solution); Figure S7: XRD patterns of the WI catalyst (left) before (top) and after (bottom) 48 h of reaction and the NN14 catalyst (right) before (top) and after (bottom) 48 h of reaction; Figure S8: The change in the glycerol conversion rate over time after 48 h of catalyst usage; Table S1: Concentration (% wt.) of each species in the NN14 catalyst and WI catalyst obtained by ICP; Table S2: Data used to calculate the crystallite size in the kinetic experiment; Table S3: Glycerol conversion, mass and carbon balance closure and product selectivity for the catalytic glycerol hydrogenolysis tests on the WI, NN14 and NN4 catalysts. Reaction conditions: T = 200 °C, P(H2) ≈ 50 bar, t = 5 h, 2.5% wt. aqueous glycerol solution, 1.5 g of catalyst, 1500 rpm magnetic stirring. Liquid products quantified by HPLC (Aminex HPX-87H column).

Author Contributions: Conceptualization: M.F. and F.G.; Methodology: M.F., F.G., G.P., M.L. and N.B.; Investigation: M.F. and F.G.; Formal analysis: M.F., M.L., C.P., I.T. and F.B.; Resources: F.G.; Data curation: M.F.; Visualization: M.F. and F.G.; Writing—original draft: M.F. and F.G.; Writing—review and editing: M.F., F.G., G.P., M.L., N.B. and C.P.; Supervision: F.G.; Funding acquisition: F.G. All authors have read and agreed to the published version of the manuscript.

Funding: This research received no external funding.

Data Availability Statement: Data available on request due to restrictions.

Acknowledgments: The authors are grateful to Andrée Lessard from the Electron Microscopy platform at the University of Sherbrooke for providing assistance in acquiring the electron micrographs supporting this study. They also thank Jesus A. V. Aguilar from McGill University for the EELS analysis. Special thanks also to Ahmed El Alaoui Laguel, who helped in the laboratory manipulations.

Conflicts of Interest: The authors declare no conflicts of interest.

Abbreviations

The following abbreviations are used in this manuscript:

1,2-PD	1,2-Propanediol
1,3-PD	1,3-Propanediol
BET	Brunauer–Emmett–Teller
BJH	Barrett–Joyner–Halenda
EG	Ethylene glycol
EELS	Electron energy loss spectroscopy
EDS	Energy-dispersive X-ray spectroscopy
FWHM	Full width at half maximum
GC	Gas chromatography
HPLC	High-performance liquid chromatography
HRTEM	High-resolution transmission electron microscopy
HVO	Hydrotreated vegetable oil
ICP	Inductively coupled plasma
MSA	Mean square average diameter
NS	Nanosheet obtained from a test
NN	Nanosheet-based catalyst
NN14	Nanosheet catalyst prepared from NS14
NN4	Nanosheet catalyst prepared from NS4
PDO	Propanediol
PTT	Polytrimethylene terephthalate
RI	Refractive index
SEM	Scanning electron microscopy
STEM	Scanning transmission electron microscopy
TCD	Thermal conductivity detector
TEM	Transmission electron microscopy
TPD	Temperature-programmed desorption
WI	Wet impregnation catalyst
XRD	X-ray diffraction
XRF	X-ray fluorescence

References

1. IEA. *Transport Biofuels—Renewables 2024*; IEA: Paris, France, 2024.
2. Kraus, G.A. Synthetic Methods for the Preparation of 1,3-Propanediol. *CLEAN Soil Air Water* **2008**, *36*, 648–651. [CrossRef]
3. Checa, M.; Nogales-Delgado, S.; Montes, V.; Encinar, J.M. Recent Advances in Glycerol Catalytic Valorization: A Review. *Catalysts* **2020**, *10*, 1279. [CrossRef]
4. Bhowmik, S.; Darbha, S. Advances in solid catalysts for selective hydrogenolysis of glycerol to 1,3-propanediol. *Catal. Rev.* **2021**, *63*, 639–703. [CrossRef]
5. García-Fernández, S.; Gandarias, I.; Requies, J.; Güemez, M.B.; Bennici, S.; Auroux, A.; Arias, P.L. New approaches to the $Pt/WO_x/Al_2O_3$ catalytic system behavior for the selective glycerol hydrogenolysis to 1,3-propanediol. *J. Catal.* **2015**, *323*, 65–75. [CrossRef]
6. Aihara, T.; Miura, H.; Shishido, T. Investigation of the mechanism of the selective hydrogenolysis of CO Checked bonds over a $Pt/WO_3/Al_2O_3$ catalyst. *Catal. Today* **2020**, *352*, 73–79. [CrossRef]
7. Aihara, T.; Miura, H.; Shishido, T. Effect of perimeter interface length between 2D WO_3 monolayer domain and gamma-Al_2O_3 on selective hydrogenolysis of glycerol to 1,3-propanediol. *Catal. Sci. Technol.* **2019**, *9*, 5359–5367. [CrossRef]

8. García-Fernández, S.; Gandarias, I.; Requies, J.; Soulimani, F.; Arias, P.L.; Weckhuysen, B.M. The role of tungsten oxide in the selective hydrogenolysis of glycerol to 1,3-propanediol over $Pt/WO_x/Al_2O_3$. *Appl. Catal. Environ.* **2017**, *204*, 260–272. [CrossRef]
9. Li, H.; Abdelgaid, M.; Paudel, J.R.; Holzapfel, N.P.; Augustyn, V.; McKone, J.R.; Mpourmpakis, G.; Crumlin, E.J. Operando Unveiling of Hydrogen Spillover Mechanisms on Tungsten Oxide Surfaces. *J. Am. Chem. Soc.* **2025**, *147*, 6472–6479. [CrossRef] [PubMed]
10. Lei, N.; Zhao, X.; Hou, B.; Yang, M.; Zhou, M.; Liu, F.; Wang, A.; Zhang, T. Effective Hydrogenolysis of Glycerol to 1,3-Propanediol over Metal-Acid Concerted $Pt/WO_x/Al_2O_3$ Catalysts. *ChemCatChem* **2019**, *11*, 3903–3912. [CrossRef]
11. Li, Z.; Wu, C.; Zhang, C.; Li, H. The Effect of WO_3 on the Selective Hydrogenolysis of Glycerol to 1,3-Propanediol over Pt/WO_3-Al_2O_3 Catalysts. *Catalysts* **2024**, *14*, 774. [CrossRef]
12. Wang, J.; Zhao, X.; Lei, N.; Li, L.; Zhang, L.; Xu, S.; Miao, S.; Pan, X.; Wang, A.; Zhang, T. Hydrogenolysis of Glycerol to 1,3-propanediol under Low Hydrogen Pressure over WOx-Supported Single/Pseudo-Single Atom Pt Catalyst. *ChemSusChem* **2016**, *9*, 784–790. [CrossRef] [PubMed]
13. Niu, Y.; Zhao, B.; Liang, Y.; Liu, L.; Dong, J. Promoting Role of Oxygen Deficiency on a WO_3-Supported Pt Catalyst for Glycerol Hydrogenolysis to 1,3-Propanediol. *Ind. Eng. Chem. Res.* **2020**, *59*, 7389–7397. [CrossRef]
14. Aihara, T.; Kobayashi, H.; Feng, S.; Miura, H.; Shishido, T. Effect of WO_3 Loading on the Activity of WO_3/Al_2O_3 Catalysts in Selective Hydrogenolysis of Glycerol to 1,3-Propanediol. *Chem. Lett.* **2017**, *46*, 1497–1500. [CrossRef]
15. Jarauta-Córdoba, C.; Bengoechea, M.O.; Agirrezabal-Telleria, I.; Arias, P.L.; Gandarias, I. Insights into the nature of the active sites of Pt-WO_x/Al_2O_3 catalysts for glycerol hydrogenolysis into 1,3-propanediol. *Catalysts* **2021**, *11*, 1171. [CrossRef]
16. García-Fernández, S.; Gandarias, I.; Tejido-Núñez, Y.; Requies, J.; Arias, P.L. Influence of the Support of Bimetallic Platinum Tungstate Catalysts on 1,3-Propanediol Formation from Glycerol. *ChemCatChem* **2017**, *9*, 4508–4519. [CrossRef]
17. Yu, Y.; Zeng, W.; Xu, M.; Peng, X. Hydrothermal synthesis of $WO_3 \cdot H_2O$ with different nanostructures from 0D to 3D and their gas sensing properties. *Phys. Low-Dimens. Syst. Nanostruct.* **2016**, *79*, 127–132. [CrossRef]
18. Zhang, N.; Li, X.; Ye, H.; Chen, S.; Ju, H.; Liu, D.; Lin, Y.; Ye, W.; Wang, C.; Xu, Q.; et al. Oxide Defect Engineering Enables to Couple Solar Energy into Oxygen Activation. *J. Am. Chem. Soc.* **2016**, *138*, 8928–8935. [CrossRef] [PubMed]
19. Chen, G.; Chu, X.; Qiao, H.; Ye, M.; Chen, J.; Gao, C.; Guo, C.Y. Thickness controllable single-crystal WO_3 nanosheets: Highly selective sensor for triethylamine detection at room temperature. *Mater. Lett.* **2018**, *226*, 59–62. [CrossRef]
20. Zhang, J.; Chen, J.; Luo, Y.; Chen, Y.; Kiani, M.; Wei, X.; Luo, R.; Wang, G.; Wang, R. Controllable synthesis of two-dimensional tungsten nitride nanosheets as electrocatalysts for oxygen reduction reaction. *Sci. China Mater.* **2018**, *61*, 1567–1574. [CrossRef]
21. Ahmed, B.; Kumar, S.; Ojha, A.K.; Donfack, P.; Materny, A. Facile and controlled synthesis of aligned WO_3 nanorods and nanosheets as an efficient photocatalyst material. *Spectrochim. Acta Part Mol. Biomol. Spectrosc.* **2017**, *175*, 250–261. [CrossRef] [PubMed]
22. Han, X.; Han, X.; Li, L.; Wang, C. Controlling the morphologies of WO_3 particles and tuning the gas sensing properties. *New J. Chem.* **2012**, *36*, 2205–2208. [CrossRef]
23. Hu, J.; Sun, Y.; Wang, X.; Chen, L.; Zhang, W.; Chen, Y. Synthesis and gas sensing properties of molybdenum oxide modified tungsten oxide microstructures for ppb-level hydrogen sulphide detection. *RSC Adv.* **2017**, *7*, 28542–28547. [CrossRef]
24. Zhang, Q.; Xu, M.; Shen, Z.; Wei, Q. A nanostructured Cr_2O_3/WO_3 p–n junction sensor for highly sensitive detection of butanone. *J. Mater. Sci. Mater. Electron.* **2017**, *28*, 12056–12062. [CrossRef]
25. He, K.; Jin, Z.; Chu, X.; Bi, W.; Wang, W.; Wang, C.; Liu, S. Fast response–recovery time toward acetone by a sensor prepared with Pd doped WO_3 nanosheets. *RSC Adv.* **2019**, *9*, 28439–28450. [CrossRef] [PubMed]
26. Xiao, J.; Song, C.; Dong, W.; Li, C.; Yin, Y. Synthesis, Characterization, and Gas Sensing Properties of WO_3 Nanoplates. *Rare Met. Mater. Eng.* **2017**, *46*, 1241–1244. [CrossRef]
27. Bandi, S.; Srivastav, A.K. Formation mechanism of nanocrystalline W derived cubic-$H_{0.5}WO_3$. *Scr. Mater.* **2022**, *208*, 114363. [CrossRef]
28. Mazur, M.; Kapuscik, P.; Weichbrodt, W.; Domaradzki, J.; Mazur, P.; Kot, M.; Flege, J.I. WO_3 Thin-Film Optical Gas Sensors Based on Gasochromic Effect towards Low Hydrogen Concentrations. *Materials* **2023**, *16*, 3831. [CrossRef] [PubMed]
29. Hatel, R.; Baitoul, M. Nanostructured Tungsten Trioxide (WO_3): Synthesis, structural and morphological investigations. *J. Phys. Conf. Ser.* **2019**, *1292*, 012014. [CrossRef]
30. Karimkhah, M.; Yourdkhani, A.; Moradpur-Tari, E.; Poursalehi, R.; Sarraf-Mamoory, R. How does water of crystallization influence the optical properties, band structure and photocatalytic activity of tungsten oxide? *Surf. Interfaces* **2021**, *27*, 101493. [CrossRef]
31. Kong, L.; Guo, X.; Xu, J.; Mo, Z.; Li, L. Morphology control of WO_3 nanoplate film on W foil by oxalic acid for photocatalytic gaseous acetaldehyde degradation. *J. Photochem. Photobiol. A Chem.* **2020**, *401*, 112760. [CrossRef]
32. Wang, Z.G.; Shen, H.Y.; Yu, R.L.; Gao, J.F.; Zhang, G.Q.; Xu, C.; Lei, J.; Du, J.G.; Xu, J.Z.; Li, Z.M. Universal production of functionalized 2D nanomaterials via integrating glucose-assisted mechanochemical exfoliation and cosolvent-intensified sonication exfoliation. *Nano Res.* **2023**, *16*, 5033–5041. [CrossRef]

33. Thummavichai, K.; Wang, N.; Xu, F.; Rance, G.; Xia, Y.; Zhu, Y. In situ investigations of the phase change behaviour of tungsten oxide nanostructures. *R. Soc. Open Sci.* **2018**, *5*, 171932. [CrossRef] [PubMed]
34. Guntida, A.; Suriye, K.; Panpranot, J.; Praserthdam, P. Lewis acid transformation to Bronsted acid sites over supported tungsten oxide catalysts containing different surface WO_x structures. *Catal. Today* **2020**, *358*, 354–369. [CrossRef]
35. Egerton, R. *Electron Energy-Loss Spectroscopy in the Electron Microscope*; Springer Nature: Berlin/Heidelberg, Germany, 2011. [CrossRef]

Disclaimer/Publisher's Note: The statements, opinions and data contained in all publications are solely those of the individual author(s) and contributor(s) and not of MDPI and/or the editor(s). MDPI and/or the editor(s) disclaim responsibility for any injury to people or property resulting from any ideas, methods, instructions or products referred to in the content.